Electrochimica Acta 527 (2025) 146106

Contents lists available at ScienceDirect

Electrochimica Acta

journal homepage: www.journals.elsevier.com/electrochimica-acta

A Pd–Pt-based bulk nanoporous alloy with continuous solubility for hydrogen

Sambit Bapari [a,c,*], Jörg Weissmüller [a,b]

[a] Institute of Materials Physics and Technology, Hamburg University of Technology, 21073 Hamburg, Germany
[b] Institute of Hydrogen Technology, Helmholtz-Zentrum Hereon, 21502 Geesthacht, Germany
[c] Department of Metallurgical and Materials Engineering, Indian Institute of Technology Ropar, Rupnagar 140001, India

ARTICLE INFO

Keywords:
Metal hydrides
Miscibility gap
Dealloying
Nanoporous
Palladium alloys

ABSTRACT

Metal hydrides that enable reversible solute exchange with a reservoir often exhibit a miscibility gap at room temperature. Misfit strain during two-phase coexistence may then lead to degradation on repeated charging/discharging cycles. Furthermore, the miscibility gap impairs continuous and uniform composition tuning for functional applications. We explore electrochemical dealloying as a pathway to macroscopic monolithic samples of nanoporous Pd–Pt with continuous solubility for H at room temperature. The ligament size is tunable in the range of 4–40 nm, and sorption isotherms suggest a miscibility-gap critical point marginally below room temperature. With a maximum hydrogen fraction of 0.5, we demonstrate a reversible actuation strain of 3.3 % and a high cycle stability.

1. Introduction

The reversible insertion and extraction of interstitial solute is the basis for many functional materials design strategies. These include prominently energy storage in metal hydrides [1,2] or in intercalation compounds, for instance, based on lithium [3–5]. They also include hydrogen-based actuators [6–10] and thermal systems [11] or materials with switchable optical transmission [12] or switchable mechanical stiffness [13,14].

Interstitials are associated with a substantial misfit strain energy, and this tends to induce miscibility gaps in the alloy phase diagram [15,16]. These gaps can be beneficial, specifically when the constant chemical potential in the two-phase region maintains a constant operating voltage in battery devices [17]. Yet, in functional applications, a miscibility gap impedes the continuous and homogeneous tuning of the solute content and, thereby, of the functionalized parameter – such as the actuation strain. This holds true even when crystal lattice coherency is maintained and the phase change takes the form of an instability [16,18–21]. More generally, the combination of misfit-induced lattice parameter change and two-phase co-existence leads to either the generation of incoherent interfaces or to coherency strain of substantial magnitude [16,22,23]. This is liable to result in stress concentration or in crystal lattice defects that accumulate over repeated charging/discharging cycles, eventually initiating failure [24–26]. It is therefore of interest to explore interstitial solutions with a large interval of continuous solubility as opposed to miscibility gaps.

Functional materials that enable reversible solute exchange with continuous solubility are well known in the field of soft matter, where hydrogels provide an example [27,28]. This is well compatible with the notion that the misfit strain energy – promoting the miscibility gap – scales with the elastic parameters [29–31] which, by definition, are weak in soft matter. In contrast, metallic interstitial solutions and specifically metal hydrides are stiff and, therefore, will typically support complete miscibility only at elevated temperature. An interesting exception are the hydrides of Pd alloyed with other transition metals, where the critical temperature of the miscibility gap can be tuned through the alloy composition [32,33]. Specifically, the system Pd–Pt–H has been well studied [34–37].

Besides enhancing the interval of solubility, the doping also allows to adjust the critical temperature near the operating temperature of the functional material. This may result in interesting phenomena, since the critical point is distinguished by a diverging solute susceptibility (composition change per change in chemical potential). In other words, large composition changes can be induced with a small driving force. This is exemplified by the suggestion of metal hydrides in which the constant-chemical-potential elastic stiffness vanishes completely at the critical point [13,14].

The present study aims at preparing a Pd–Pt based metal hydride with a critical temperature at or below room temperature and with a large continuous solubility interval for H. Our study is inspired by

---

* Corresponding author at: Department of Metallurgical and Materials Engineering, Indian Institute of Technology Ropar, Rupnagar 140001, India.
E-mail addresses: sambit.bapari@iitrpr.ac.in, sambit.bapari@tuhh.de (S. Bapari).

https://doi.org/10.1016/j.electacta.2025.146106
Received 8 February 2025; Received in revised form 16 March 2025; Accepted 24 March 2025

earlier work on nanoporous Pd–H, which can be made in the form of load-bearing monolithic and samples, suitable as actuators [6,8,10] or as load-bearing functional elements with switchable stiffness [13]. Even though these materials take the form of 3D macroscopic bodies, they can exhibit sensibly fast and controlled equilibration with hydrogen in an external reservoir [8,10]. The addition of Pt has been studied in the context of dealloying Ag-Au, where added Pt – owing to its slow surface diffusion – suppresses coarsening and affords microstructures with extremely small characteristic length scale [38–43].

Here, we present a protocol for doping of np-Pd with Pt, and we demonstrate that the critical point of the miscibility gap is reduced to below room temperature. The wide interval of continuous solid solubility and the absence of the phase transformation are accompanied by a high cycle stability.

2. Materials and methods

Master alloy ingots $Cu_{85}(Pd_{95}Pt_5)_{15}$ were prepared by melting the 99.995% pure constituents. The ingots, 2.5 g in mass, were sealed in evacuated quartz tubes and homogenized at 1173 K for 120 h, then rolled down to 1.7 mm thick discs. Intermediate anneals at 1073 K for 600 s after every 20% reduction in thickness and a final anneal afforded recovery. A diamond wire saw served to section the discs into 0.9 mm × 0.9 mm × 1.7 mm master alloy specimens.

A three electrode setup with a Ag/AgCl pseudo reference electrode (∼ 0.51 V vs the standard hydrogen electrode, SHE) and a potentiostat (PGSTAT-302N) were used in all electrochemical processes. The pseudo reference electrodes were calibrated against a commercial SHE in the respective working electrolyte. All electrode potentials (E_{SHE}) reported in this article are with respect to SHE. Counter electrodes were coiled Cu wire (99.9%) for dealloying and porous carbon cloth for electrochemical characterization. Dealloying and other electrochemical processes were carried out in 1M H_2SO_4 aqueous electrolyte that was prepared by dilution of commercially available concentrated H_2SO_4 (Sigma-Aldrich) with deionized water. Pairs of master alloy samples were dealloyed together at a constant potential.

In situ dilatometry used a miniaturized three-electrode cell in a vertical dilatometer. The contact pressure was 0.1 MPa and the temperature was $T = 296\,\mathrm{K}$.

Scanning electron microscopy (SEM) used a Zeiss Supra 55VP FEG SEM, equipped with an Oxford X-Max 20 SDD Energy Dispersive X-ray (EDX) detector. For cross-sectional characterization, samples were notched with a scalpel and then cleaved. The software ImageJ (v1.53k) [44] was used to measure line distances in the micrographs.

Transmission electron microscopy (TEM) used a FEI Talos F200X TEM equipped with a high brightness Schottky field-emission gun and four silicon drift detectors for EDX. Specimens for TEM were crushed to powder (by gentle compression and shear) and dispersed on molybdenum grids. The electron-transparent areas from the edges of the nanoporous powder particles were analyzed.

Small-angle X-ray scattering (SAXS) used a point focus instrument (Xenocs Xeuss 3.0) with a copper microfocus source (Genix 3D), a fully evacuated beam path, and a 2D solid-state detector (Pilatus 300 K). Scattering data from two sample-detector distances were combined for an interval 0.05–10 nm^{-1} in wave number, q. Further details can be found in [45].

Coarsening was induced by isothermal anneals in an infrared furnace (ULVAC MILA-5000) at a vacuum $< 2 \times 10^{-6}\,\mathrm{mbar}$. The specimens were initially wet with ethanol; this was allowed to evaporate in-furnace before ramping up the temperature. This step was implemented to minimize the amount of adsorbed water on the pore surfaces. Annealing temperature was varied in the range of 423–673 K, keeping a fixed heating rate 0.7 K/s optimized for crack free microstructures.

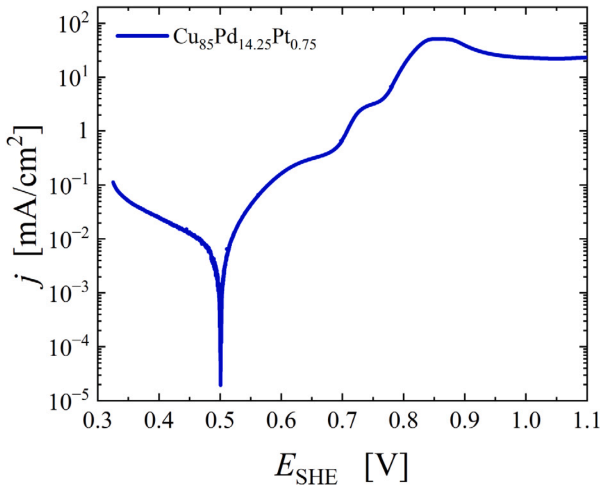

Fig. 1. Polarization plot with the master alloy $Cu_{85}Pd_{14.25}Pt_{0.75}$ in 1M H_2SO_4. Current density (current normalized to the external surface area), j, versus the electrode potential, E_{SHE}, against a standard hydrogen electrode (SHE), at potential scan rate $\dot{E}_{\mathrm{SHE}} = 1$ mV/s.

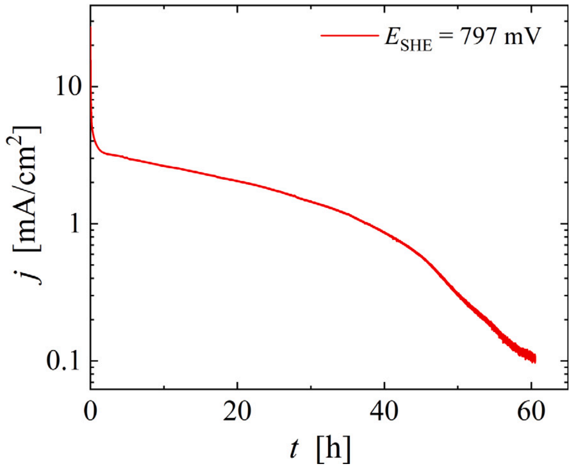

Fig. 2. Constant potential dealloying of $Cu_{85}Pd_{14.25}Pt_{0.75}$. Current density (per area of external surface) j, on logarithmic scale, vs dealloying time, t, during dealloying in 1M H_2SO_4 at dealloying potential $E_{\mathrm{SHE}} = 797$ mV.

3. Results

3.1. Dealloying

Dealloying in the present study aimed at macroscopic, load bearing bodies of nanoporous Pd, alloyed with transition metals to bring the critical temperature of the hydride miscibility gap to near ambient. We choose Pt as the extra transition metal and Cu as the sacrificial element. Cu, Pd and Pt form a continuous series of solid solutions [46]. Cu has > 0.5 V difference in standard electrode potential relative to both, Pd and Pt. Based on an earlier dealloying study of Cu–Pd [47], we found 85 at.% Cu and dealloying in 1M H_2SO_4 electrolyte adequate for complete dealloying of the ternary master alloy and for obtaining load-bearing monolithic samples. In the polarization plot for the master alloy, Fig. 1, the current density, j (defined as current per area of external surface), reflects the dissolution rate of the less noble element. Extensive mapping of the process-parameter space led to a protocol with a constant dealloying potential of 797 mV in 1M H_2SO_4 at 296 K. A steep initial current transient then evolves into a sustained dealloying current density around $2\,\mathrm{mA/cm}^2$, see Fig. 2. The sustained current density is consistent with reports suggesting that a minimum of $1\,\mathrm{mA/cm}^2$

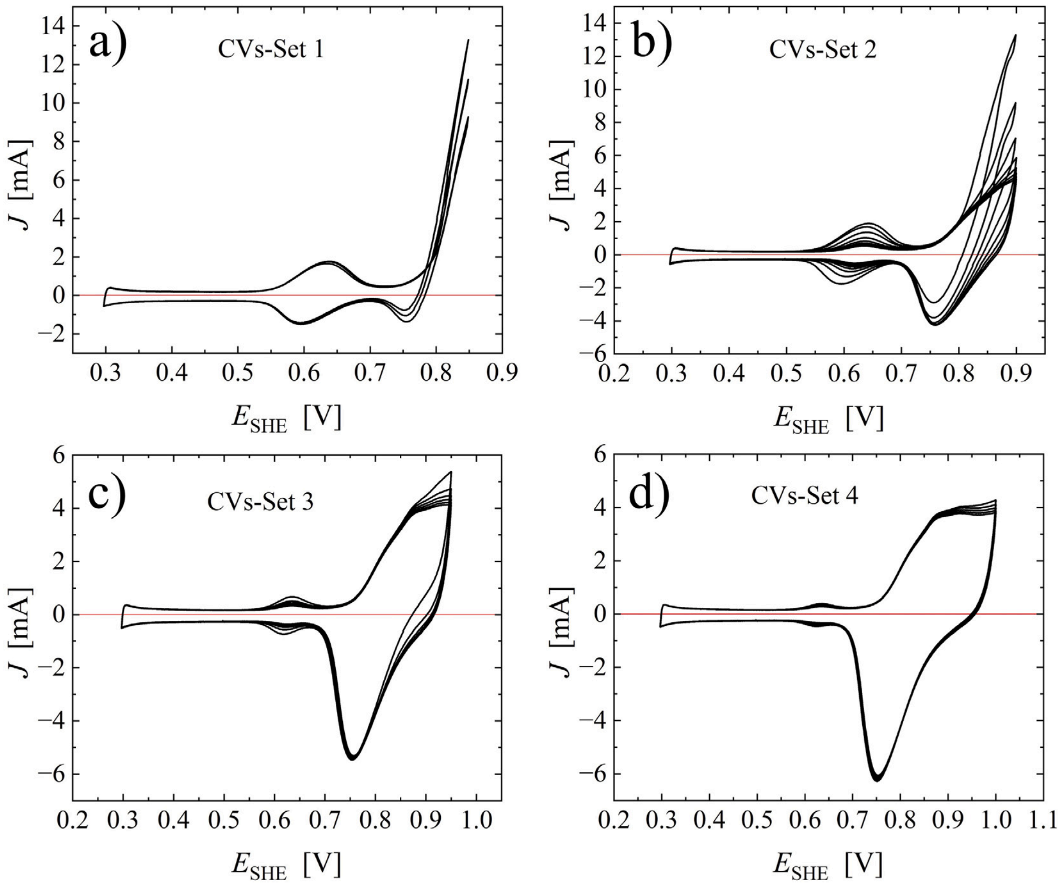

Fig. 3. Post-dealloying cyclic voltammograms (CVs) in 1M H_2SO_4. Sets of CVs, with E_{SHE} in the range of (a) 0.30–0.85 V, (b) 0.30–0.9 V, (c) 0.30–0.95 V, and (d) 0.30–1.00 V, in succession. Scan rate was consistently $\dot{E}_{SHE} = 0.7\,\mathrm{mVs^{-1}}$ at $T = 296\,\mathrm{K}$.

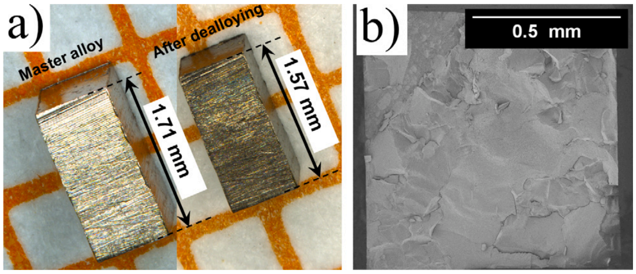

Fig. 4. Macroscale morphology of the specimens. (a) Optical images of master alloy specimen on the left, same specimen in nanoporous state after dealloying on the right. Shrinkage is exemplified by indicated change in specimen length. (b) Scanning electron micrograph of a fracture surface of as dealloyed np-PdCuPt.

is required for complete dealloying of bulk specimens [48,49]. In our study, significantly lower or higher starting current densities resulted in surface passivation or specimen disintegration, respectively. The constant-potential dealloying continued for 60 h. Longer dealloying (at lesser dealloying potential) led to coarsening, while completing the dealloying within a day (at higher dealloying potential) led to severe cracking.

The constant-potential part of the dealloying was considered complete when the current had decayed to $10\,\mu\mathrm{A}$. Next, we executed repeated potential cycles in a fresh electrolyte. That procedure reduces the residual less-noble element content [47,50]. Guided again by the strife to mitigate crack formation, we choose potential intervals confined within 0.3–1.0 V and the scan rate as 0.7 mV/s. Specifically, multiple sets of CVs in succession of increasing upper potential limits 0.85 (4 cycles), 0.90 (8 cycles), 0.95 (6 cycles) and 1.0 V (5 cycles) with a fixed lower vertex at 0.3 V were implemented. Fig. 3(a-d) show the associated CVs. In the interval $E_{SHE} = 600 - 650\,\mathrm{mV}$, peaks during anodic and cathodic scanning indicate Cu dissolution and redeposition, respectively. Those peaks gradually diminish, indicating Cu removal. The last cycle was terminated at 0.4 V to achieve an adsorbate-free surface.

Drying conditions were optimized for preventing disintegration due to capillarity-induced stresses [51]. After cleaning in deionized water, each dealloyed specimen was transferred to ethanol that was again replaced by n-pentene after 10 h. Specimens wet with n-pentene were dried in air after 6 h.

Using the above recipe, np-PdCuPt could be prepared with high reproducibility. An average linear shrinkage of $\sim 8\%$ was observed after dealloying as exemplified in Fig. 4a. The specimens were millimeter-size monoliths, free of cracks, as evident from the micrograph of the fracture surface of an as-dealloyed specimen in Fig. 4b.

3.2. Microstructure and composition

Fig. 5a shows a typical SEM micrograph of the fracture surface for as-dealloyed specimens. The extremely small ligament size prevents a quantitative, SEM-based analysis of the characteristic microstructural length scale. In the TEM images at higher resolution, the three-dimensional network structure prevents clear identification of all individual ligament segments in the projected two-dimensional images. However, two clearly identifiable exemplary ligament segments with diameters of 5.2 and 3.8 nm are indicated in Fig. 5b and c, respectively. These TEM images exemplify the typical nanostructure of dealloyed specimens that were investigated with an average ligament diameter of 4–5 nm.

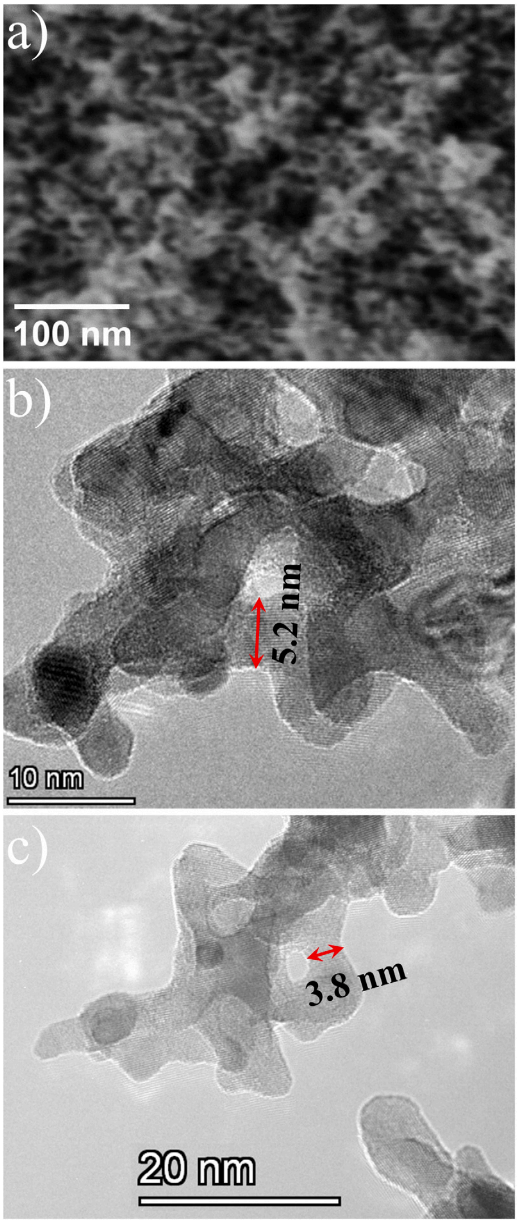

Fig. 5. Microstructure of as dealloyed np-PdCuPt. (a) Scanning electron micrograph, (b,c) transmission electron microscopy bright field images. Exemplary ligament diameters are marked in red. Note the difference in scale bars.

EDX analysis shows Pd, Cu and Pt at 86.3 ± 0.5, 9.0 ± 0.5 and 4.7 ± 0.1 at% respectively, when probed at various locations in the cross sections of the batch of samples used in this study. For conciseness, we shall refer to the nanoporous material with that composition as np-PdCuPt. Based on mass and lateral dimensions, the solid fraction, φ, was determined as 0.22 ± 0.01.

The TEM-imaged elemental distribution is shown in Fig. 6. The features displayed in the HAADF-STEM image resemble those in maps of the Pd and Pt atom fraction. This suggests homogeneous intermixing of those two constituents. By contrast, Cu appears concentrated as Cu-rich clusters in the interior of the ligaments. This can be understood as residual Cu atoms that were never exposed to the surface for dissolution, resembling Ag-rich clusters in nanoporous Au [52–54].

Fig. 7 exemplifies microstructures of np-PdCuPt exposed to four different annealing states. It is seen that annealing prompts coarsening, from the initial 4 nm up to 40 nm, an entire order of magnitude in ligament size. Our attention is on fast sorption kinetics and, consequently, on extremely fine microstructural length scales. With this in mind, the remainder of this study focuses on the as-prepared material, ignoring the sample qualities of the coarse structures.

3.3. Characteristic length scale in the as-prepared state

As described above, the TEM study reveals a ligament diameter in the order of $L_\mathrm{W} \approx 4 - 5\,\mathrm{nm}$. For a characterization with a stronger statistical basis, we have investigated the porous material with SAXS. This approach is sensitive to the spacing, $\tilde{L}$, between neighboring ligaments [50]. $\tilde{L}$ can be inferred from the SAXS interference peak's wavenumber, q_0, according to [45,55]

$$\tilde{L} \approx 1.23 \times 2\pi / q_0 \,. \qquad (1)$$

The small-angle scattering data in Fig. 8a shows a weak hump but no clear interference peak. The signature of microstructural correlation is more pronounced in the Kratky plot (showing the scattering power function $4\pi q^2 I(q)$ versus q) in Fig. 8b. With a peak at $q_0 \approx 0.59\,\mathrm{nm}^{-1}$, Eq. (1) here gives $\tilde{L} \approx 13\,\mathrm{nm}$.

A conversion factor between $\tilde{L}$ and L_W depends on φ. It can be estimated by extrapolating data in [50] to the slightly lesser solid fraction φ of the present study; this yields $\tilde{L}/L_\mathrm{W} = 3.05$. When combined with the SAXS data for $\tilde{L}$, the conversion factor suggests $L_\mathrm{W} = 4.3\,\mathrm{nm}$, in good agreement with the TEM observation.

3.4. Hydrogen sorption isotherms

Fig. 9 exemplifies cyclic voltammograms (CV) characterizing the electrode processes on np-PdCuPt in 1 M H_2SO_4. Differently shaded regions mark the potential intervals of dominantly hydrogen underpotential deposition (here with a small contribution from the onset of bulk absorption), capacitive charging, and oxygen species adsorption.

Hydrogen sorption isotherms of hydrogen atom fraction (amount of H per amount of Pd), x_H, versus electrode potential E were determined by current integration, exploiting the electron transfer in $\mathrm{H}^+ + e^- \leftrightharpoons H$. Hydrogen absorption in the bulk is distinguished from underpotential deposition (UPD) by differences in the strain-per-H coupling coefficient [8,57]. In situ dilatometry enabled monitoring of the coupling. This experiment provided the basis for discriminating between adsorption (UPD) and absorption, which is manifest in a sharp change in the graph of strain versus transferred charge (see Fig S1 in the Supporting Information). As our study focuses on the bulk sorption isotherms, we corrected the total amount of H for absorption; thus, our data for x_H only accounts for the bulk absorbed H.

Fig. 10 shows sorption isotherms at $T = 296\,\mathrm{K}$ based on CVs at different scan rates. The cathodic vertex potential was never inferior to $E_\mathrm{SHE} = 0.005\,\mathrm{V}$, so as to mitigate molecular hydrogen evolution. Indeed, the CV graphs are closed, indicating negligible loss of hydrogen by that process. The maximum hydrogen fraction is found as 0.5. The CVs exhibit substantial hysteresis, which diminishes with decreasing scan rate.

In order to explore sorption isotherms closer to equilibrium, we measured the hydrogen uptake in staircase voltammetry, with step intervals adjusted for complete equilibration. Fig. 11 shows the resulting bulk sorption isotherm. Here, hysteresis is practically absent, and instead the absorption and desorption branches are in excellent agreement. The in situ dilatometry traces, Fig. 12a, of sorption-induced length change versus time during similar potential-time programs provide further support for equilibration.

It is noteworthy that the sorption isotherms include stable hydrogen fractions throughout the entire composition regime $x_\mathrm{H} = 0 - 0.5$. This suggests continuous solubility in this regime, and the absence of a miscibility gap. The almost complete lack of hysteresis in Fig. 11 confirms this observation. The steep composition variation near $x_\mathrm{H} = 0.2$ suggests that the experiment temperature is close to the critical temperature.

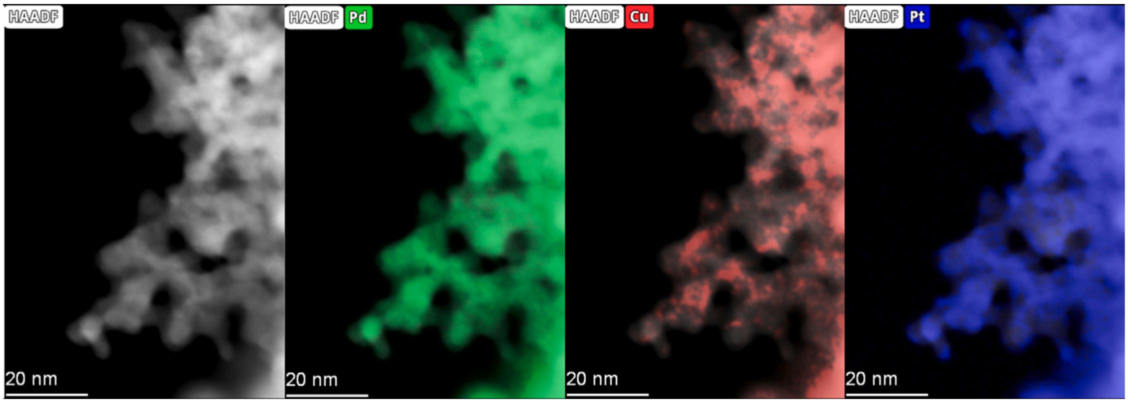

Fig. 6. Element-resolved transmission electron micrographs of np-PdCuPt. High-angle annular dark-field scanning transmission electron microscopy images and corresponding superimposed elemental maps of Pd (green), Cu (red) and Pt (blue).

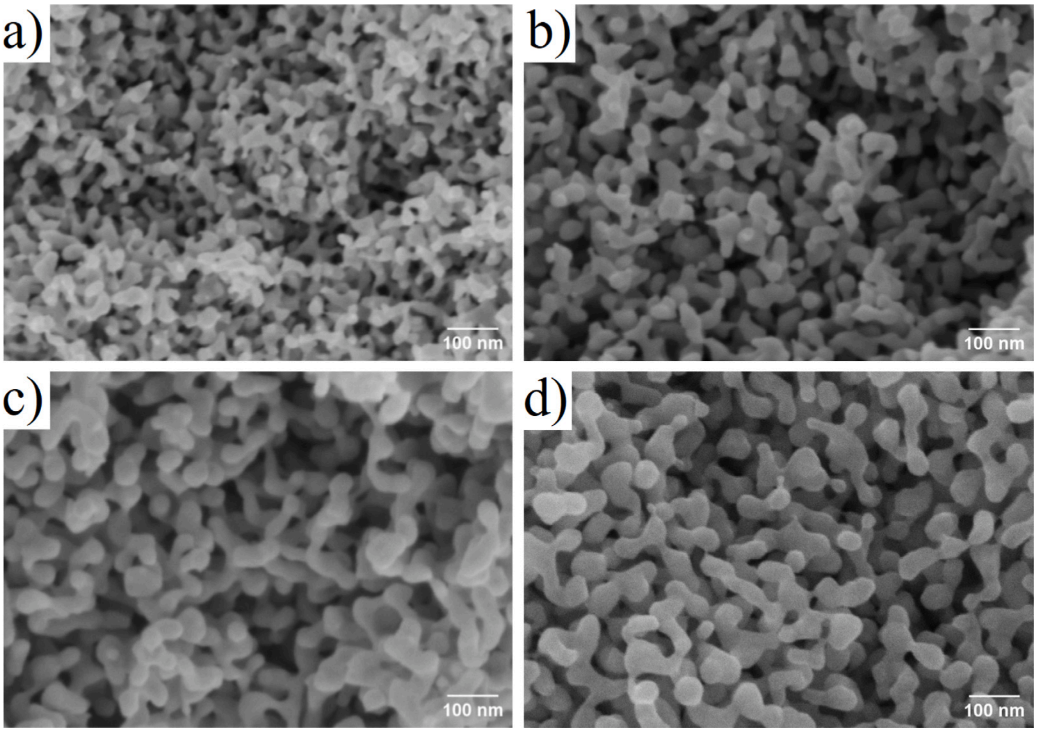

Fig. 7. Scanning electron micrographs showing cleavage surfaces of np-PdCuPt at various states of annealing at (a) 523 K for 1 h, (b) 573 K for 1 h, (c) 573 K for 2 h and (d) 623 K for 1.5 h.

A noteworthy feature of the stepwise desorption data in Fig. 12a is a strong variation of the equilibration time, $t_{1/2}$, with E_{SHE}. By $t_{1/2}$ we understand the time required to achieve half the total length change after a potential step. Fig. 12b represents the $t_{1/2}$ for the staircase profile of Fig. 12a in a log-linear plot. The equilibration is slowest for intermediate hydrogen fraction, in the range $E_{\mathrm{SHE}} = 45 - 55\,\mathrm{mV}$, with $t_{1/2}$ around 1000 s. The equilibration is significantly faster in dilute and concentrated solutions.

The slow equilibration at around 50 mV can be understood as the key factor for the hysteresis observed in the CVs. In other words, even the smallest scan rate in Fig. 10 does not provide adequate time for equilibration near the critical region of the miscibility gap. The data from the stepwise potential variation and equilibration confirm complete solute solubility in spite of the hysteresis during continuous potential scans.

3.5. Cycling stability

With an eye on characterizing cycling stability, we have subjected a sample to repeated hydrogen charging/discharging cycles while monitoring the length change. Each cycle consisted of 400 s at −210 mV, followed by 200 s at 400 mV. Similar protocols would be involved if the material was assessed as an actuator. The experiment was stopped after six days, at which point 835 cycles had been completed.

Fig. 13 documents the results of the cycling experiment. The dominant signature of the time-dependent length change, Fig. 13a, is reversible expansion and contraction with an (actuation) strain amplitude $\gtrsim 3\%$ and sensibly complete equilibration after each potential step.

Superimposed to the cyclic strain is an irreversible contraction, which is slow after the first 50 cycles. Its overall magnitude after 835 cycles was 1.8%. This included 1.1% in the first 50 cycles and only 0.7% in the remaining 785 cycles. This is a substantially lesser irreversible change than observed with np Pd–H in a similar protocol [8].

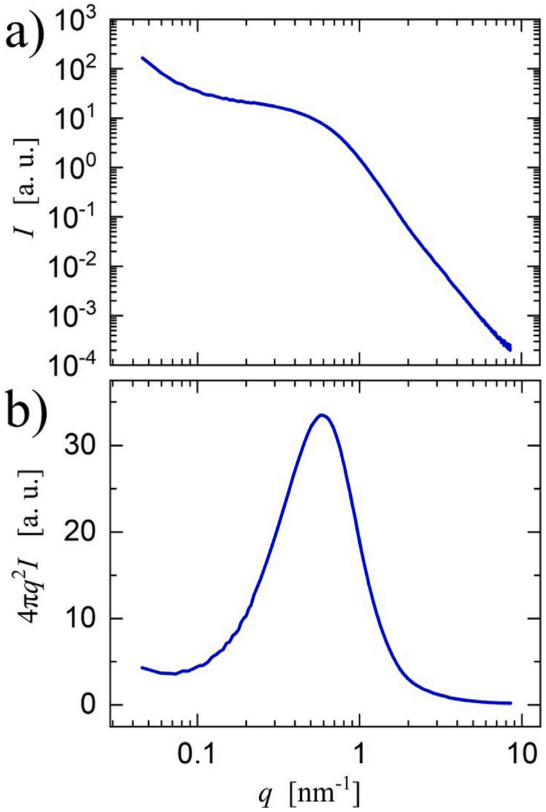

Fig. 8. Small-angle X-ray scattering data, showing (a) intensity I and (b) Kratky plot [56] of I multiplied by $4\pi q^2$ versus wave number q in a log scale for a powdered np-PdCuPt specimen. Note the different ordinate scales in (a) and (b).

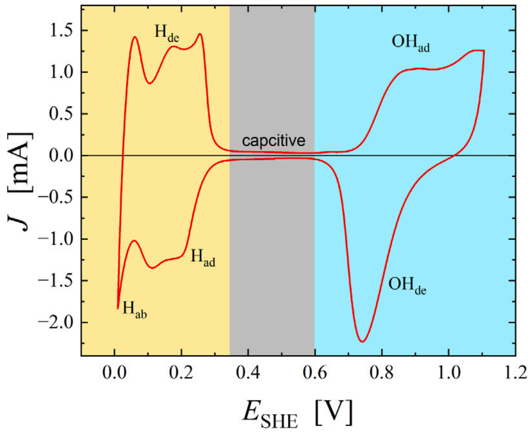

Fig. 9. Cyclic voltammogram of np-PdCuPt. Electrode current, J, versus electrode potential E_{SHE} at scan rate $\dot{E}_{SHE}$ = 1 mV/s. Shaded regions delineate (from left to right) hydrogen underpotential deposition (here with a small contribution from the onset of bulk absorption), capacitive charging, and oxygen species adsorption.

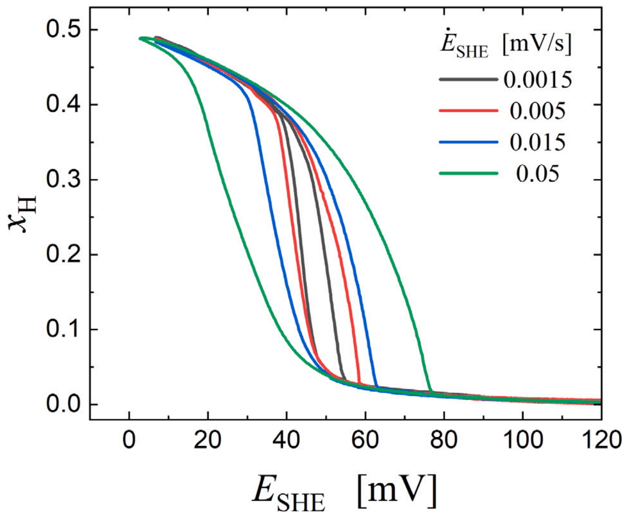

Fig. 10. Sorption isotherms of hydrogen fraction x_H versus electrode potential E_{SHE} during cyclic voltammetry at different scan rates, as indicated by color code and legends.

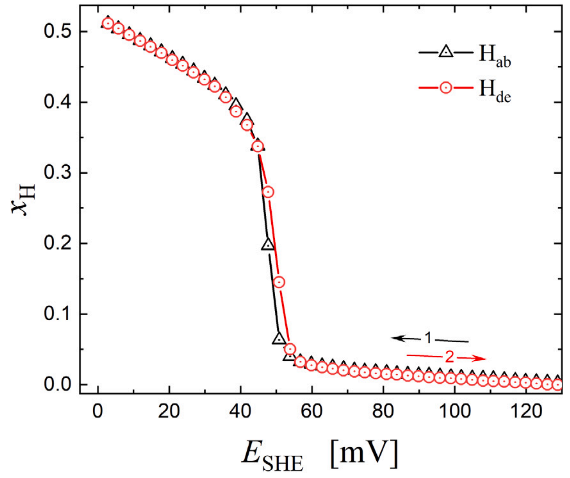

Fig. 11. Sorption isotherm, measured during stepwise equilibration at discrete values of electrode potential. Hydrogen fraction x_H variation during absorption (black, H_{ab}) and desorption (red, H_{de}), plotted as function of electrode potential E_{SHE}. Colored arrows with numbers indicate that absorption was followed by desorption as E_{SHE} was varied stepwise, first decreasing and then increasing. Note that there is no evidence for a miscibility gap, and that hysteresis is practically absent.

As a measure for the sorption kinetics, the inset in Fig. 13b shows the halftimes, $t_{1/2}$, for the length change to saturate during absorption and desorption. It may be noted that for the 2nd cycle, $t_{1/2}$ of absorption and desorption was 79 s and 75 s, respectively. While the absorption halftime remained sensibly constant, the desorption halftime diminished with the cycle number, reaching 42 s in the 835th cycle.

Fig. 13c shows the evolution of the actuation amplitude with the cycle number. Note that the strain amplitude (true) of each cycle is referred to the current sample length, avoiding a cross-coupling between irreversible contraction and reversible cyclic length change. Remarkably, the amplitude increases during cycling, from 2.8% to 3.3% (Fig. 13c). Most of the increase occurs during the first 50 cycles. A conceivable explanation is that the potential cycles are accompanied by surface diffusion, which exposes previously buried Cu to the surface, enabling further dissolution. The analogous process is well documented for secondary dealloying [52,54]. As the electrode potential of Cu^{2+}/Cu^0 is 340 mV [58], the applied 400 mV is indeed sufficient for dissolving Cu. Because Cu reduces the solubility for H, the amount of hydrogen exchanged then increases, and so does the strain amplitude.

4. Discussion and conclusions

Our study aimed at a metal hydride with fast internal equilibration kinetics and continuous solid solubility for hydrogen at room temperature, in a wide composition regime. We choose nanoporous (np) $Pd_{95}Pt_5$ as a target material for which the critical temperature of

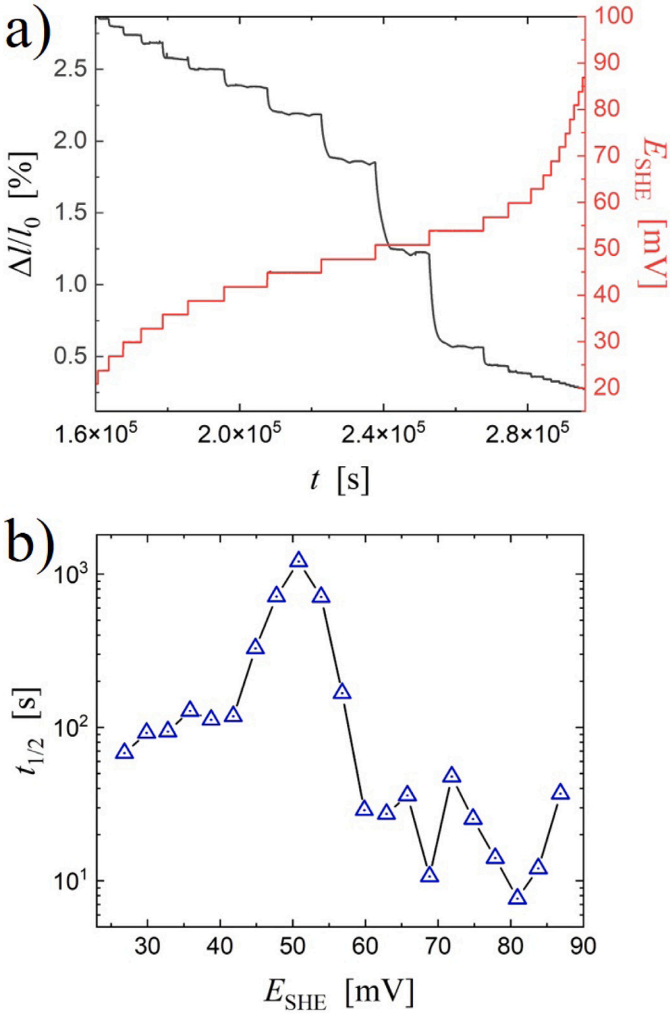

Fig. 12. (a) Dilatometry during stepwise desorption. Red graph and right ordinate: electrode potential versus time, t. Black graph and left ordinate: relative length change, $\Delta l/l_0$ versus t. (b) Halftime, $t_{1/2}$, for individual potential steps of the staircase profile in (a) plotted on a logarithmic scale against applied potential E_{SHE}.

the miscibility gap is near room temperature [35,37]. Dealloying the precursor $Pd_{85}Cu_{14.25}Pt_{0.75}$ resulted in np $Pd_{86}Cu_9Pt_5$.

Dealloying our ternary precursor is challenging due to the small potential window between the critical dealloying potential and the onset of platinum oxidation. Our protocol is based on optimized constant-potential dealloying followed by potential cycles in different intervals and a dedicated post-dealloying drying procedure. The protocol supplies monolithic samples with the ligament size as small as 4 nm. Contrary to earlier reports [8] on np Pd made by dealloying Pd-Cu, the as-prepared state exhibits a single characteristic length scale rather than a two-scale, hierarchical microstructure. Coarsening allows to increase the size up to at least 40 nm.

Pd and Pt are thoroughly mixed in the bulk of the ligaments, yet Cu-rich regions persist after dealloying. Those regions are consistent with observations on clusters, rich in the sacrificial element, in dealloyed np Au [52,53,59]. A slight increase in the strain amplitude during adsorption/desorption cycles is consistent with increasing hydrogen solubility and, thereby, with decreasing Cu content after extended cycling.

Sorption isotherms measured during cyclic voltammetry at room temperature indicate hysteresis even at potential scan rates as small as $50\,\mu\mathrm{V/s}$. Yet, stepwise sorption isotherms admitting even more time for equilibration confirm that our np PdCuPt can be charged continuously with H up to $x_{\mathrm{H}} = 0.5$, with no miscibility gap.

The absence of the miscibility gap implies that hydrogen sorption avoids two-phase states. Indeed, our observation of a remarkable cycle stability during charging/discharging cycles is consistent with low damage accumulation. This supports the notion that lattice defects – which might result from coherency stresses or incoherent interfaces in two-phase states – are avoided.

The slow equilibration in a composition–temperature regime that we argue to be near the critical point of the miscibility gap is remarkable. As we find the equilibration time $t_{1/2}$ strongly dependent on the bulk composition, $t_{1/2}$ appears to reflect processes within the solid. Indeed, transport in the electrolyte and adsorption are not expected rate limiting – the effective proton transport in the pore space, by the Grotthuss mechanism, can be expected fast, and data for the equilibration between the hydrogen UPD layer on Pt and acidic electrolyte indicates a characteristic time $< 1\,\mathrm{ms}$ [60]. Bulk diffusion also appears unlikely as a rate-limiting step – the high diffusivity of H in the bulk of the nanoscale ligaments suggests an extremely short characteristic time for internal equilibration, again on the order of $1\,\mathrm{ms}$ [13]. We might therefore hypothesize that the rate-limiting step behind our $t_{1/2} > 1000\,\mathrm{s}$ near criticality is the transfer of H between adsorption- and absorption sites. That step, an established subprocess in hydriding transition metals [61], would then encounter a barrier within the crystal interior. Ongoing work in our team aims to verify this hypothesis, using impedance spectroscopy and exploring the variation of the exchange current density with the equilibrium hydrogen fraction, as it is selected by the electrode potential. On that basis, and accounting for the nature of metal hydrides as solid solutions with a strong solute–solute interaction, the underlying rate equation might be documented and compared to the Butler–Volmer equation [62,63] or to current-overpotential equations based on it [64]. Those equations provide a standard approach to the sorption kinetics of H in Pd [65–68].

To summarize, the present study demonstrates a nanoporous metal hydride with a large interval of continuous solid solubility for hydrogen at room temperature. The absence of a miscibility gap avoids the accumulation of crystal lattice defects during repeated charging/discharging cycles. The remarkable cycle stability in our study supports this notion. Furthermore, the continuous solubility may be of interest in hydrogen-driven functional materials, where it affords tuning the hydrogen fraction continuously and uniformly in a wide interval.

CRediT authorship contribution statement

Sambit Bapari: Writing – review & editing, Writing – original draft, Methodology, Investigation, Formal analysis, Conceptualization. **Jörg Weissmüller:** Writing – review & editing, Supervision.

Declaration of competing interest

The authors declare that they have no known competing financial interests or personal relationships that could have appeared to influence the work reported in this paper.

Acknowledgment

This work was supported by the German Research Foundation (DFG) through grant WE1424/18-1.

Appendix A. Supplementary data

Supplementary material related to this article can be found online at https://doi.org/10.1016/j.electacta.2025.146106.

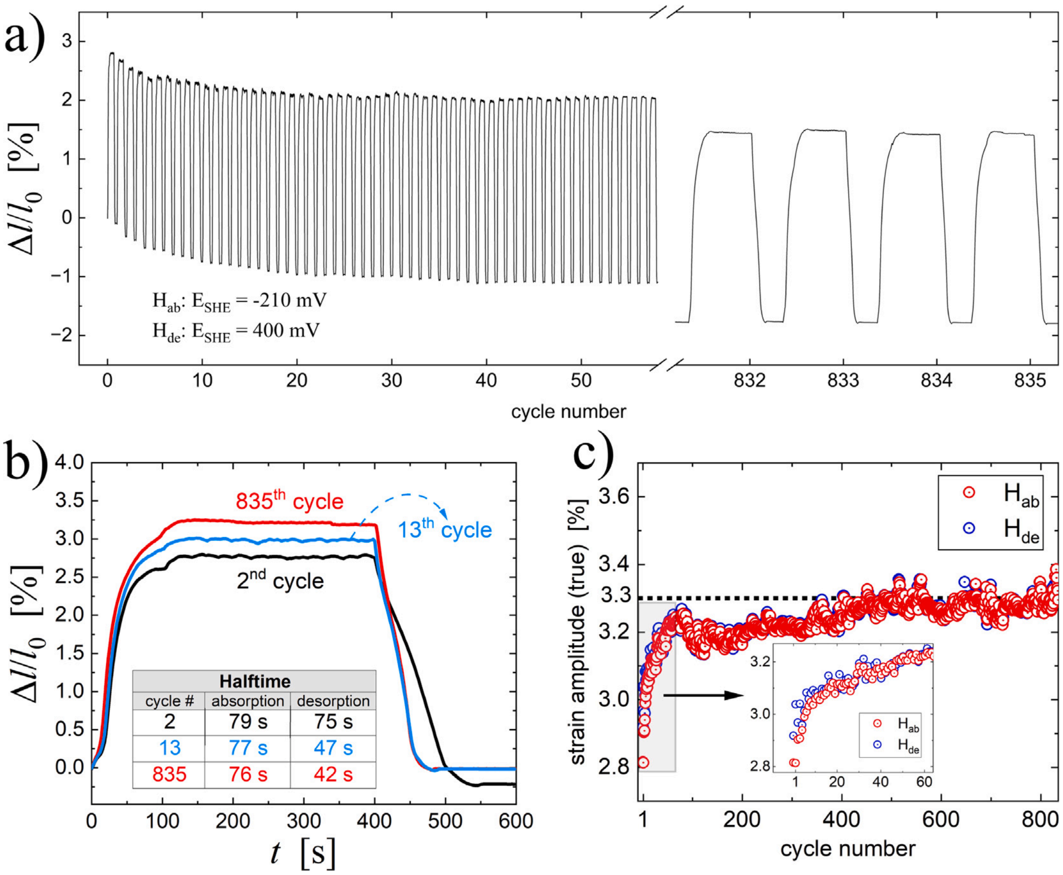

Halftime		
cycle #	absorption	desorption
2	79 s	75 s
13	77 s	47 s
835	76 s	42 s

Fig. 13. Hydrogen-assisted actuation with np-PdCuPt in 1M H_2SO_4. (a) Length change $\Delta l/l_0$ versus time (encoded by cycle number; 600 s per cycle) during > 800 cycles. Each cycle includes electrode potential E_{SHE} at −210 mV for 400 s (H-absorption) and then at 400 mV for 200 s (H-desorption). (b) Strain variation with time, t, for 2nd (black), 13th (blue) and 835th (red) cycles. Corresponding halftimes for adsorption and desorption are tabulated. (c) Strain amplitude (true) for adsorption (red) and desorption (blue) vs. cycle number. Magnified inset figure shows strain amplitudes for first 60 cycles. Dashed horizontal line marks final true strain amplitude value, 3.3%.

Data availability

Data will be made available on request.

References

[1] Y. Shang, C. Pistidda, G. Gizer, T. Klassen, M. Dornheim, Mg-based materials for hydrogen storage, J. Magnes. Alloy. 9 (6) (2021) 1837–1860.

[2] N. Klopčič, I. Grimmer, F. Winkler, M. Sartory, A. Trattner, A review on metal hydride materials for hydrogen storage, J. Energy Storage 72 (2023) 108456.

[3] J. Dodd, R. Yazami, B. Fultz, Phase diagram of Li_xFePO_4, Electrochem. Solid-State Lett. 9 (3) (2006) A151.

[4] C. Delacourt, P. Poizot, J.-M. Tarascon, C. Masquelier, The existence of a temperature-driven solid solution in Li_xFePO_4 for $0 \le x \le 1$, Nat. Mater. 4 (3) (2005) 254–260.

[5] P. Bai, D.A. Cogswell, M.Z. Bazant, Suppression of phase separation in $LiFePO_4$ nanoparticles during battery discharge, Nano Lett. 11 (11) (2011) 4890–4896.

[6] J. Zhang, Q. Bai, Z. Zhang, Dealloying-driven nanoporous palladium with superior electrochemical actuation performance, Nanoscale 8 (13) (2016) 7287–7295.

[7] E.-M. Steyskal, C. Wiednig, N. Enzinger, R. Würschum, In situ characterization of hydrogen absorption in nanoporous palladium produced by dealloying, Beilstein J. Nanotechnol. 7 (2016) 1197–1201.

[8] S. Shi, J. Markmann, J. Weissmüller, Actuation by hydrogen electrosorption in hierarchical nanoporous palladium, Phil. Mag. 97 (19) (2017) 1571–1587.

[9] M. Gößler, E.-M. Steyskal, M. Stütz, N. Enzinger, R. Würschum, Hydrogen-induced plasticity in nanoporous palladium, Beilstein J. Nanotechnol. 9 (2018) 3013–3024.

[10] F. Tan, B. Yu, Y. Wang, Q. Bai, Z. Zhang, Hierarchically structured nanoporous palladium with ordered/disordered channels for ultrahigh and fast strain, Nano Lett. 23 (2) (2023) 505–513.

[11] K. Malleswararao, P. Dutta, S. Murthy S., Applications of metal hydride based thermal systems: A review, Appl. Therm. Eng. 215 (2022) 118816.

[12] J. Huiberts, R. Griessen, J. Rector, R. Wijngaarden, J. Dekker, D. De Groot, N. Koeman, Yttrium and lanthanum hydride films with switchable optical properties, Nature 380 (6571) (1996) 231–234.

[13] S. Shi, J. Markmann, J. Weissmüller, Verifying Larché-Cahn elasticity, a milestone of 20th-century thermodynamics, Proc. Natl. Acad. Sci. 115 (43) (2018) 10914–10919.

[14] J. Weissmüller, S. Shi, Giant compliance and spontaneous buckling of beams containing mobile solute atoms, Acta Mater. 227 (2022) 117696.

[15] P. Fratzl, O. Penrose, Ising model for phase separation in alloys with anisotropic elastic interaction—I. Theory, Acta Met. et Mater. 43 (8) (1995) 2921–2930.

[16] J. Weissmüller, Coherent phase change in interstitial solutions: A hierarchy of instabilities, Adv. Sci. (2024) 2308554.

[17] S.K. Dhar, S.R. Ovshínsky, P.R. Gifford, D.A. Corrigan, M.A. Fetcenko, S. Venkatesan, Nickel/metal hydride technology for consumer and electric vehicle batteries—A review and up-date, J. Power Sources 65 (1) (1997) 1–7.

[18] R. Schwarz, A. Khachaturyan, Thermodynamics of open two-phase systems with coherent interfaces: Application to metal–hydrogen systems, Acta Mater. 54 (2) (2006) 313–323.

[19] S. Wagner, H. Uchida, V. Burlaka, M. Vlach, M. Vlcek, F. Lukac, J. Cizek, C. Baehtz, A. Bell, A. Pundt, Achieving coherent phase transition in palladium–hydrogen thin films, Scr. Mater. 64 (10) (2011) 978–981.

[20] D.B. Ravnsbæk, K. Xiang, W. Xing, O.J. Borkiewicz, K.M. Wiaderek, P. Gionet, K.W. Chapman, P.J. Chupas, Y.M. Chiang, Extended solid solutions and coherent transformations in nanoscale olivine cathodes, Nano Lett. 14 (3) (2014) 1484–1491.

[21] Y. Li, J. Weissmüller, Size-dependent phase change in energy storage materials: Comparing the impact of solid-state wetting and of coherency stress, J. Chem. Phys. 162 (2) (2025).

[22] S. Wagner, P. Klose, V. Burlaka, K. Nörthemann, M. Hamm, A. Pundt, Structural phase transitions in niobium hydrogen thin films: Mechanical stress, phase equilibria and critical temperatures, ChemPhysChem 20 (14) (2019) 1890–1904.

[23] A. Dyck, T. Böhlke, A. Pundt, S. Wagner, Phase transformation in the palladium hydrogen system: Effects of boundary conditions on phase stabilities, Scr. Mater. 247 (2024) 116117.

[24] A. Ulvestad, M. Welland, W. Cha, Y. Liu, J. Kim, R. Harder, E. Maxey, J. Clark, M. Highland, H. You, et al., Three-dimensional imaging of dislocation dynamics during the hydriding phase transformation, Nat. Mater. 16 (5) (2017) 565–571.

[25] G. Bucci, B. Talamini, A. Renuka Balakrishna, Y.-M. Chiang, W.C. Carter, Mechanical instability of electrode-electrolyte interfaces in solid-state batteries, Phys. Rev. Mater. 2 (10) (2018) 105407.

[26] Y. Zhao, P. Stein, Y. Bai, M. Al-Siraj, Y. Yang, B.-X. Xu, A review on modeling of electro-chemo-mechanics in lithium-ion batteries, J. Power Sources 413 (2019) 259–283.

[27] L. Ionov, Hydrogel-based actuators: possibilities and limitations, Mater. Today 17 (10) (2014) 494–503.

[28] W. Feng, Z. Wang, Tailoring the swelling-shrinkable behavior of hydrogels for biomedical applications, Adv. Sci. 10 (28) (2023) 2303326.

[29] J.D. Eshelby, The Continuum Theory of Lattice Defects, vol. 3, Academic Press, 1956, pp. 79–144.

[30] J.W. Cahn, On spinodal decomposition, Acta Metall. 9 (9) (1961) 795–801.

[31] P. Fratzl, O. Penrose, J.L. Lebowitz, Modeling of phase separation in alloys with coherent elastic misfit, J. Stat. Phys. 95 (5–6) (1999) 1429–1503.

[32] E. Wicke, H. Brodowsky, H. Züchner, Hydrogen in palladium and palladium alloys, in: J. Alefeld (Ed.), Hydrogen in Metals II: Application-Oriented Properties, Springer, Berlin, Heidelberg, 1978, pp. 73–155.

[33] T.B. Flanagan, S. Luo, Thermodynamics of hydrogen solution and hydride formation in binary Pd alloys, J. Phase Equilibria Diffus. 28 (1) (2007) 49–57.

[34] B. Baranowski, F.A. Lewis, W.D. McFall, S. Filipek, T.C. Witherspoon, A.R.J.P. Ubbelohde, A study of the palladium–platinum–hydrogen system over a wide range of hydrogen pressures, Proc. R. Soc. A 386 (1791) (1997) 309–332.

[35] T. Yasumatsu, J.L. Wan, M. Matsuyama, K. Watanabe, Absorption of hydrogen isotopes by Pd–Pt alloys, J. Alloys Compd. 293–295 (1999) 900–907.

[36] I. Moysan, V. Paul-Boncour, S. Thiébaut, E. Sciora, J.M. Fournier, R. Cortes, S. Bourgeois, A. Percheron-Guégan, Pd-Pt alloys: correlation between electronic structure and hydrogenation properties, J. Alloys Compd. 322 (1) (2001) 14–20.

[37] K. Hubkowska, M. Łukaszewski, A. Czerwiński, Influence of temperature on hydrogen electrosorption into palladium-noble metal alloys. Part 2—Palladium–platinum alloys, Electrochim. Acta 56 (5) (2011) 2344–2350.

[38] J.T. Zhang, H.Y. Ma, D.J. Zhang, P.P. Liu, F. Tian, Y. Ding, Electrocatalytic activity of bimetallic platinum-gold catalysts fabricated based on nanoporous gold, Phys. Chem. Chem. Phys. 10 (22) (2008) 3250–3255.

[39] J. Snyder, P. Asanithi, A.B. Dalton, J. Erlebacher, Stabilized nanoporous metals by dealloying ternary alloy precursors, Adv. Mater. 20 (24) (2008) 4883–4886.

[40] H.J. Jin, X.L. Wang, S. Parida, K. Wang, M. Seo, J. Weissmüller, Nanoporous Au-Pt alloys as large strain electrochemical actuators, Nano Lett. 10 (1) (2010) 187–194.

[41] A.A. Vega, R.C. Newman, Nanoporous metals fabricated through electrochemical dealloying of Ag-Au-Pt with systematic variation of Au:Pt ratio, J. Electrochem. Soc. 161 (1) (2013) C1–C10.

[42] A.A. El-Zoka, J.Y. Howe, R.C. Newman, D.D. Perovic, In situ STEM/SEM study of the coarsening of nanoporous gold, Acta Mater. 162 (2019) 67–77.

[43] M. Liu, J. Weissmüller, Phase decomposition in nanoporous Au-Pt, Acta Mater. 241 (2022) 118419.

[44] C.A. Schneider, W.S. Rasband, K.W. Eliceiri, NIH Image to ImageJ: 25 years of image analysis, Nature Methods 9 (7) (2012) 671–675.

[45] L. Riedel, J. Markmann, J. Weissmüller, S. Shi, Tailoring hierarchical nanoporous gold on dual length scales, Phys. Rev. Mater. 7 (11) (2023) 116001.

[46] A. Potekaev, A. Klopotov, M. Starostenkov, V. Klopotov, T. Markova, M. Morozov, Structure-phase states in the Cu–Pd-Pt system, Steel Transl. 43 (4) (2013) 184–187.

[47] S. Shi, J. Markmann, J. Weissmüller, Synthesis of uniform bulk nanoporous palladium with tunable structure, Electrochim. Acta 285 (2018) 60–69.

[48] K. Sieradzki, N. Dimitrov, C. McCall, N. Vasiljevic, J. Erlebacher, The dealloying critical potential, J. Electrochem. Soc. 149 (8) (2002) B370.

[49] K. Sieradzki, Curvature effects in alloy dissolution, J. Electrochem. Soc. 140 (10) (1993) 2868.

[50] S. Bapari, L. Lührs, J. Weissmüller, Metrics for the characteristic length scale in the random bicontinuous microstructure of nanoporous gold, Acta Mater. (2023) 119333.

[51] G. Wittstock, M. Bäumer, W. Dononelli, T. Klüner, L. Lührs, C. Mahr, L.V. Moskaleva, M. Oezaslan, T. Risse, A. Rosenauer, et al., Nanoporous gold: From structure evolution to functional properties in catalysis and electrochemistry, Chem. Rev. 123 (10) (2023) 6716–6792.

[52] T. Krekeler, A.V. Straßer, M. Graf, K. Wang, C. Hartig, M. Ritter, J. Weissmüller, Silver-rich clusters in nanoporous gold, Mater. Res. Lett. 5 (5) (2017) 314–321.

[53] C. Mahr, P. Kundu, A. Lackmann, D. Zanaga, K. Thiel, M. Schowalter, M. Schwan, S. Bals, A. Wittstock, A. Rosenauer, Quantitative determination of residual silver distribution in nanoporous gold and its influence on structure and catalytic performance, J. Catalysis 352 (2017) 52–58.

[54] Y. Li, B.-N. Ngo-Dinh, J. Markmann, J. Weissmüller, Evolution of length scales and of chemical heterogeneity during primary and secondary dealloying, Acta Mater. 222 (2022) 117424.

[55] P. Debye, H.R. Anderson, H. Brumberger, Scattering by an inhomogeneous solid. II. The correlation function and its application, J. Appl. Phys. 28 (6) (1957) 679–683.

[56] A.G. Kikhney, D.I. Svergun, A practical guide to small angle X-ray scattering (SAXS) of flexible and intrinsically disordered proteins, FEBS Lett. 589 (19, Part A) (2015) 2570–2577.

[57] R. Viswanath, J. Weissmüller, Electrocapillary coupling coefficients for hydrogen electrosorption on palladium, Acta Mater. 61 (16) (2013) 6301–6309.

[58] B. Ershov, Electrode potentials involving atoms and ions of metals in intermediate oxidation states in aqueous solutions, J. Mol. Liq. 402 (2024) 124770.

[59] A.A. El-Zoka, B. Langelier, G.A. Botton, R.C. Newman, Enhanced analysis of nanoporous gold by atom probe tomography, Mater. Charact. 128 (2017) 269–277.

[60] B.E. Conway, L. Bai, Determination of adsorption of OPD H species in the cathodic hydrogen evolution reaction at Pt in relation to electrocatalysis, J. Electroanal. Chem. Interfacial Electrochem. 198 (1) (1986) 149–175.

[61] G. Jerkiewicz, Hydrogen sorption at/in electrodes, Prog. Surf. Sci. 57 (2) (1998) 137–186.

[62] E.J. Dickinson, A.J. Wain, The Butler-Volmer equation in electrochemical theory: Origins, value, and practical application, J. Electroanal. Chem. 872 (2020) 114145.

[63] S. Fletcher, Butler–Volmer meets microscopic reversibility, Curr. Opin. Electrochem. 37 (2023) 101199.

[64] A.J. Bard, L.R. Faulkner, Electrochemical Methods. Fundamentals and Applications, second ed., Wiley, New York, 2001.

[65] J.S. Chen, J.P. Diard, R. Durand, C. Montella, Hydrogen insertion reaction with restricted diffusion. Part 1. Potential step—EIS theory and review for the direct insertion mechanism, J. Electroanal. Chem. 406 (1) (1996) 1–13.

[66] J.-W. Lee, S.-I. Pyun, Anomalous behaviour of hydrogen extraction from hydride-forming metals and alloys under impermeable boundary conditions, Electrochim. Acta 50 (9) (2005) 1777–1805.

[67] C. Montella, Comments on the review ‘Anomalous behaviour of hydrogen extraction from hydride-forming metals and alloys under impermeable boundary conditions’, by J.-W. Lee, S.-I. Pyun, Electrochim. Acta 50 (2005) 1777–1805; Electrochim. Acta 51 (2005) 361–373.

[68] M. Simhofer, P. Brunner, J. Weissmüller, R. Würschum, Diffusion–reaction modelling of modulated hydrogen loading, Phil. Mag. 104 (15–16) (2024) 647–680.